Modal analysis of flame-generated nanoparticle dynamics in confined turbulent swirling flows

Jinbo Cheng, Wang Han,* Yihao Tang, and Lijun Yang
School of Astronautics, Beihang University, Beijing 100191, China

(Received 2 September 2025; accepted 10 June 2026; published 29 June 2026)

Flame-generated nanoparticles, such as soot, caused by the incomplete combustion of hydrocarbon fuels in reacting flows, have adverse effects on human health and the environment. Understanding the interaction between soot and flow dynamics is critical to reducing particle emissions from engine combustors. This is because soot formation and evolution are highly sensitive to the flow dynamics encountered, especially in confined turbulent swirling flows, where strong shear layers and recirculation regions introduce complex, coherent patterns of both fast and slow timescales. These patterns are often crucial for understanding soot evolution and for controlling its formation and emission. To this end, large-eddy simulations (LES) of an aeroengine model combustor, with and without dilution jets, are conducted using state-of-the-art soot models. Then, modal analysis of flow and soot dynamics in the combustor is performed using the spectral proper orthogonal decomposition (SPOD) method with transient LES data. To the best of the authors' knowledge, this work is the first study to utilize SPOD and raw LES data to reveal the dynamics of coherent structures in swirl sooting flames. The frequency bands of both high-frequency dynamics (HFD, 234.375–468.75 Hz) and low-frequency dynamics (LFD, 0–156.25 Hz) are identified without any *prior* filtering. It is found that HFD primarily exists in the shear layer and inner recirculation zone, whereas LFD is present throughout the entire combustor. Compared to LFD, the HFD has a significant impact on velocity and gas-phase soot precursors (PAH), while LFD plays a crucial role in soot evolution. Furthermore, the results show that the evolution of velocity, PAH, and soot is closely coupled within the LFD frequency band. It is found that for soot and PAH, the impact of dilution jets on HFD modes is minor and on LFD modes is significant, while the opposite trend is observed for velocity modes.

DOI: 10.1103/n58c-d86t

I. INTRODUCTION

In reacting flows, the presence of incomplete burning of hydrocarbon fuels can lead to the generation of polycyclic aromatic hydrocarbons (PAHs), which ultimately results in the formation of solid particles (i.e., soot) with complicated nanoscale structures and diameters of a few tens of nanometers [1,2]. These soot particles are typically considered the dominant particle type, having a warming effect on global climate by absorbing and scattering solar radiation and modifying cloud properties [3,4]. In addition, as an undesirable byproduct of combustion, soot particles are significant contributors to PM1.0, which poses a threat to human health [5,6]. In this context, understanding soot dynamics in turbulent reacting flows is critical to reducing particle emissions from engine combustors.

*Contact author: drwanghan@buaa.edu.cn

Previous investigations have concluded that the physiochemical processes that contribute to soot formation and evolution exhibit high sensitivity to flow dynamics encountered [1,7–15]. It is expected that there exist complex interactions between flow dynamics and soot dynamics in confined turbulent swirling flows relevant to aeroengine combustors due to the presence of strong shear layers and recirculation zones, which will introduce fast time-scale and slow time-scale coherent structures. The precessing vortex core (PVC) near the high-speed shear layers is a fast time-scale process and comparable to the timescale of chemistry [16], which is considered energetically dominant coherent structures [11,17–19] and exhibits periodic axial precession with a certain frequency. Previous studies have shown that PVC can affect swirling flames in various ways. For instance, it can enhance fuel/air mixing [20–23] and the mixing of burned and unburned gas [24,25] as well as roll-up, stretch or local quenching of reaction zones [16,25]. Typically, the PVC is also related to thermoacoustic instabilities [26,27]. However, the recirculation zones are slow time-scale motions, with characteristic timescales on the order of tens of milliseconds [28]. This is comparable to the timescales associated with the polymerization and growth of gas-phase PAHs [29] as well as the formation of solid-phase soot particles. In this context, these low-frequency dynamics have a more significant impact on soot formation than PVC.

To this end, a few studies have investigated the influence of coherent structures on soot evolution in aeroengine model combustors. Geigle *et al.* [7] experimentally demonstrated that the PVC structure has a notable impact on soot formation in a pressurized DLR dual-swirl combustor [8]. Eberle *et al.* [9] performed a numerical investigation of transient soot evolution in the combustor and reported that the PVC can enhance the mixing of fuel, primary air, and hot burned gas from the inner recirculation zone (IRZ), thereby helping flame stabilization and influencing soot formation. Chong *et al.* [10] conducted a spectral analysis by placing probe points in the IRZ, outer recirculation zone (ORZ), and shear layers, to explore the dominant frequencies of velocity and soot volume fraction. They found that soot formation could be decoupled from the dominant flow modes in certain regions of the flow due to the inherently nonperiodic and highly intermittent fluctuations of soot evolution. Grader *et al.* [11] concluded that there exist low-frequency dynamics in swirl combustors, and they found that low-frequency velocity disturbances occur in the entire swirling flow field, which is the main reason for the intermittent evolution of soot.

As a huge amount of numerical and experimental data becomes available, data-driven modal decomposition techniques play increasingly vital roles in understanding the dynamics of coherent structures in turbulent flows [30–32], in which a well-known technique is proper orthogonal decomposition (POD) proposed by Lumley [33,34]. For POD, the flow field is decomposed into modes based on differences in energy levels, each of which can be regarded as a time-varying flow structure with a specific energy amplitude. Based on POD, several variants have been proposed [30–32,35], including dynamic mode decomposition [36], multi-scale proper orthogonal decomposition [37], spectral proper orthogonal decomposition [33,34,38], etc. Nonetheless, the application of modal decomposition in turbulent sooting flames is relatively rare. Recently, Geigle *et al.* [7] conducted POD analysis on instantaneous experimental measurement data and found that the PVC-dominated mode has a significant impact on soot formation and oxidation. Litvinov *et al.* [39] employed POD and phase-averaging techniques to identify PVC in the inner shear layer and double helical vortex in the outer shear layer of swirling flames. The results indicated that the vortex-induced roll-up of fuel is the main process occurring at isothermal conditions.

More recently, with the help of high-fidelity large-eddy simulation (LES) data, Grader *et al.* [11] used multiresolution proper orthogonal decomposition (MRPOD) to investigate the effects of low-frequency dynamics (LFD) and high-frequency dynamics (HFD) (i.e., PVC dynamics) on soot evolution in a model aeroengine combustor. They concluded that both LFD and HFD affect soot evolution, and that HFD contributes less than LFD. It is noted that in Ref. [11] the LFD and HFD are isolated by artificially predetermining the nominal bandpass of [0, 125] Hz and [375, 625] Hz, respectively, due to the lack of continuous distribution of modal energy in time–frequency space within the framework of MRPOD. Furthermore, the impact of the dilution jets on the LFD and HFD is not considered in that work.

TABLE I. Applications of SPOD [38] in representative flow configurations.

Flow configurations	References	Flow configurations	References
Pipe	[40]	Flow around object	[41–43]
Boundary layer	[44,45] [48,49]	Channel flow	[46,47] [50,51]
Mixing layer	[52,53]	Bubbly flow	[54,55]
Jet	[56,57] [61,62]	Wake	[58–60] [30,63]
	[64–66]	Nonsooting flame	[17,67]
	[68,69]	Sooting flame	This work

Identifying the dominant frequencies of complex coherent patterns that evolve in time and space is the main goal of dynamical systems theory. This motivates the authors to employ the state-of-the-art spectral proper orthogonal decomposition (SPOD) technique to identify coherent structures in the DLR combustor. SPOD was introduced by Lumley [33,34] and further developed by Towne *et al.* [38], which combines the advantages of conventional POD and dynamic mode decomposition. Moreover, SPOD is capable of optimally accounting for the random nature of turbulent flows and provides the continuous distribution of modal energy in time–frequency space. Recently, SPOD has been utilized in various flow configurations, which are broadly summarized in Table I.

With this background, the objective of this work is threefold: (1) to identify LFD and HFD in the aeroengine model combustor using the SPOD method, (2) to investigate the impact of LFD and HFD on soot dynamics, and (3) to explore the role of dilution jets in soot evolution from the perspective of modal analysis.

To achieve the above objective, the DLR FIRST combustor (see Fig. 1) is employed in this work as an aeroengine model combustor to perform modal analysis of flow dynamics and soot dynamics in the confined turbulent swirling flow. This is because substantial experimental data on the combustor

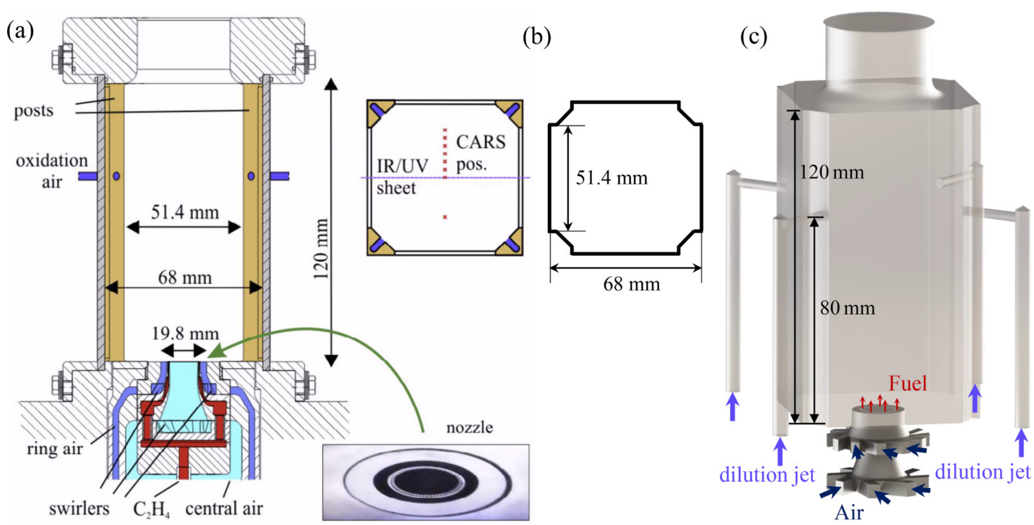

FIG. 1. (a) Sketch of the experimental configuration from Geigle *et al.* [70]. (b) Cross section of the DLR FIRST combustor. (c) Three-dimensional geometry of the DLR FIRST combustor.

TABLE II. Operating conditions for the cases considered here.

Pressure (bar)	$Q_{\text{air,central}}$ (slpm)	$\text{Re}_{\text{air,central}}$	$Q_{\text{air,ring}}$ (slpm)	$\text{Re}_{\text{air,ring}}$	Q_{fuel} (slpm)	Q_{dilution} (slpm)	Re_{total}	Φ_{global}
5	234.2	29 600	546.2	27 500	65.4	0	67 800	1.2
5	234.2	29 600	546.2	27 500	65.4	312.1	67 800	0.86

are available at elevated pressures of 3 bar and 5 bar, which can be used to validate the numerical models. To minimize NOx emissions from the combustor, the fuel is first burned with a fraction of the total air at the upstream locations, thereby minimizing NOx emissions. The remaining air is introduced quickly at the downstream locations, which is referred to as rich quench lean (RQL) combustion concept. In this context, in RQL, soot particles formed upstream can be oxidized as far downstream as possible to ensure that as few as possible leave the combustor. Therefore, the DLR-FIRST combustor can be used to investigate the influence of dilution jets downstream on soot formation. In this work, the high-fidelity LESs of the DLR-FIRST combustor under high pressure of 5 bar, are performed, considering two operating conditions with and without dilution jets. A series of instantaneous sequence signals of physical quantities is obtained at a high sampling frequency. The presence of PVC can be discerned from the instantaneous velocity field, and the highly intermittent evolution of soot can be detected from a series of sequential signals.

In the remaining paper, the operating conditions and simulation setups will be introduced in Sec. II; the SPOD formulation will be explained in Sec. III; the results are presented in Sec. IV, where the feasibility of SPOD in dealing with such highly intermittent problem is proven with successful identifications of the coherent structures associated with various frequencies and the analysis of the influence of the corresponding structures on soot evolution is made; the paper is finished with conclusions in Sec. V.

II. SIMULATION DETAILS

In this section, the geometric structure of the DLR FIRST combustor is described first. Then, the key physicochemical processes involved in soot formation and evolution in a swirl combustor are demonstrated. Finally, the LES-based modeling framework is presented.

A. Experimental configuration

The DLR FIRST combustor proposed by Geigle *et al.* [8] is considered in this work to investigate the influence of flow dynamics on soot evolution. As shown in Fig. 1, the combustor has a square cross-section of 68 × 68 mm^2 with a height of $h = 120$ mm. The primary air is supplied by a dual radial swirler at a temperature of 298 K. The nozzle diameter of the central swirler is 12.3 mm, while the inner and outer diameters of the ring swirler are 14.4 mm and 19.8 mm, respectively. Ethylene (C_2H_4) is injected through 60 square nozzles (fuel nozzle area = 0.5 × 0.4 mm^2) which are located between these two swirling air streams. In addition to the primary air inlets, there are four secondary air (or dilution jet) injection ports with a diameter of 5 mm located 80 mm from the bottom of the combustor to mimic the RQL concept. In this work, the experimental cases with and without dilution jets at the pressure of 5 bar are investigated. The operating conditions for the two cases are given in Table II. To demonstrate the experimental configurations, Fig. 2 shows the rendering of instantaneous temperature isosurfaces ($T = 1350$ K) for cases with and without dilution jets. It is observed that when four air dilution jets are injected into the combustor, air-rich zones form downstream, which can facilitate soot oxidation.

B. Soot formation and evolution

Soot formation and evolution involve complex processes that contain many physical and chemical subprocesses. As shown in Fig. 3, these processes can be divided into two major categories:

FIG. 2. Instantaneous temperature isosurfaces ($T = 1350$ K) for cases without (left) and with (right) dilution jets.

the formation and collision of gas-phase precursors, and a series of physicochemical reactions in the solid phase. Specifically, the gas-phase reactions include those of small molecules and large aromatic hydrocarbons, while the solid-phase physicochemical reactions include nucleation, coagulation, condensation, surface growth, oxidation, and fragmentation of soot particles. It is noted

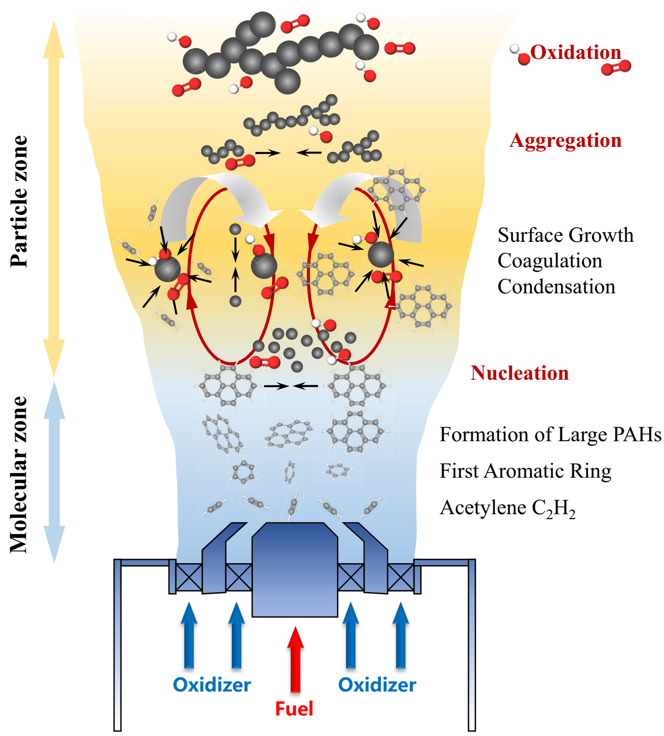

FIG. 3. Schematic of soot formation and evolution in turbulent swirling flows [71].

that the above processes occur at high temperatures, with a timescale of milliseconds. In this context, it is challenging to capture and model the processes of soot formation and evolution in turbulent reacting flows.

C. Modeling framework

In this work, the LES approach combined with state-of-the-art soot models is used to investigate the impact of flow dynamics on soot formation and evolution. In LES, large-scale eddy structures are resolved, while small-scale eddies and their impact on large-scale structures are modeled. Within the framework of LES, the Favre-filtered quantity of a scalar ϕ is calculated as

$$\widetilde{\phi}(\boldsymbol{x},t) = \frac{1}{\overline{\rho}}\int_{-\infty}^{+\infty} \rho(\boldsymbol{y},t)\phi(\boldsymbol{y},t)G(\boldsymbol{y}-\boldsymbol{x})d\boldsymbol{y}, \tag{1}$$

where t is time, $\boldsymbol{x}$ the vector of spatial coordinates, ρ the density, and $\overline{\rho}$ the filtered density. G is a filter kernel, typically assumed to be a box filter defined by the computational grid [72]. The filtered equations can be obtained by applying the above filtering operation to the instantaneous Navier-Stokes equations as follows

$$\frac{\partial \overline{\rho}}{\partial t} + \frac{\partial \overline{\rho}\widetilde{u}_j}{\partial x_j} = 0, \tag{2}$$

$$\frac{\partial \overline{\rho}\widetilde{u}_i}{\partial t} + \frac{\partial \overline{\rho}\widetilde{u}_i\widetilde{u}_j}{\partial x_j} = -\frac{\partial \overline{p}}{\partial x_i} + \frac{\partial \sigma_{ij}}{\partial x_j} + \frac{\partial \sigma_{ij}^{sgs}}{\partial x_j}, \tag{3}$$

where $\widetilde{u}_j$ is the Favre-filtered velocity component, and $\overline{p}$ is the filtered hydrodynamic pressure. σ_{ij} is the filtered viscous stress tensor with

$$\sigma_{ij} = 2\widetilde{\mu}\widetilde{S}_{ij} = \widetilde{\mu}\left(\frac{\partial \widetilde{u}_i}{\partial x_j} + \frac{\partial \widetilde{u}_j}{\partial x_i} - \frac{2}{3}\frac{\partial \widetilde{u}_k}{\partial x_k}\delta_{ij}\right) \tag{4}$$

and $\sigma_{ij}^{sgs} = \overline{\rho}\widetilde{u}_i\widetilde{u}_j - \overline{\rho}\widetilde{u_i u_j}$ is the subfilter stress tensor which is modeled using a dynamic Smagorinsky model suggested by Germano *et al.* [73] within the framework of eddy viscosity assumption.

Besides the turbulence model, performing LES of soot formation and evolution still requires three submodels: (a) a model for gas-phase chemistry, (b) a model for turbulent-chemistry interaction, and (c) a model for the evolution of soot particles. For the gas-phase chemistry modeling, both finite-rate chemistry [9,11,74,75] and tabulated chemistry [12,76–78] are widely used in the combustion community. It is found that the tabulated chemistry is able to reconcile the computational cost and accuracy reasonably [13,79]. In this context, tabulated chemistry is employed in this work to describe gas-phase chemistry within the framework of LES. To include radiation effects, the radiation flamelet/progress variable (RFPV) approach [12,15,80–82] is employed in this work, in which the full thermochemical state variables are mapped into a reduced-order space containing three scalars, i.e., mixture fraction Z, progress variable C, and heat loss parameter H. The corresponding governing equations for the three scalars are given by

$$\frac{\partial \overline{\rho}\widetilde{Z}}{\partial t} + \frac{\partial \overline{\rho}\widetilde{u}_i\widetilde{Z}}{\partial x_j} = \frac{\partial}{\partial x_j}\left(\overline{\rho}(D+D_t)\frac{\partial \widetilde{Z}}{\partial x_j}\right) + \widetilde{S_Z}\,, \tag{5}$$

$$\frac{\partial \overline{\rho}\widetilde{C}}{\partial t} + \frac{\partial \overline{\rho}\widetilde{u}_i\widetilde{C}}{\partial x_j} = \frac{\partial}{\partial x_j}\left(\overline{\rho}(D+D_t)\frac{\partial \widetilde{C}}{\partial x_j}\right) + \widetilde{S_C}\,, \tag{6}$$

$$\frac{\partial \overline{\rho}\widetilde{H}}{\partial t} + \frac{\partial \overline{\rho}\widetilde{u}_i\widetilde{H}}{\partial x_j} = \frac{\partial}{\partial x_j}\left(\overline{\rho}(\alpha+\alpha_t)\frac{\partial \widetilde{H}}{\partial x_j}\right) + \widetilde{S_H} + \widetilde{Q}_{\mathrm{rad}}, \tag{7}$$

where D and α are mass diffusivity and thermal diffusivity, respectively, which can be retrieved using the tabulated chemistry table. D_t and α_t are eddy diffusivity. $\widetilde{Q}_{\mathrm{rad}}$ is the radiation source term, which is modeled using the optically thin approach with absorption coefficients following Barlow *et al.* [83]. It is noted that the coefficients in all of the subgrid models are evaluated using the dynamic procedure and that the unity Lewis number assumption (i.e., $\alpha = D$ and $\alpha_t = D_t$) is used in this work. Since the mass fractions of PAH and the mass transfer rate from the gas phase to soot cannot be accurately characterized by the steady flamelet solutions due to slow PAH chemistry, the following spatially filtered transport equation for a lumped PAH mass fraction is transported instead of directly taking the mass fraction from the table:

$$\frac{\partial \overline{\rho} \widetilde{Y_{\mathrm{PAH}}}}{\partial t} + \frac{\partial \overline{\rho} \widetilde{u}_i \widetilde{Y_{\mathrm{PAH}}}}{\partial x_j} = \frac{\partial}{\partial x_j}\left(\overline{\rho}(D + D_t)\frac{\partial \widetilde{Y_{\mathrm{PAH}}}}{\partial x_j}\right) + \widetilde{S_{Y_{\mathrm{PAH}}}}, \tag{8}$$

where the source term $\widetilde{S_{Y_{\mathrm{PAH}}}}$ is obtained following the work of Refs. [81] and [15] using a scale-similarity assumption.

$\widetilde{S_Z}$, $\widetilde{S_C}$, and $\widetilde{S_H}$ are source terms that are also retrieved from the chemistry table. In sooting flames, PAH are removed from the gas-phase during soot formation. This removal locally alters the elemental composition, such that the mixture fraction is no longer a strictly conserved scalar. To account for this effect, a source term is added into the mixture fraction equation, which is defined analogously to the element mass fraction-based mixture fraction of Bilger [84]. Furthermore, the progress variable is defined by its own transport equation [Eq. (6)] rather than by the conventional sum of major product mass fractions, since PAH removal alters the local H/C ratio and the local effective fuel composition. A normalizing factor is therefore introduced to account for the modified stoichiometry, and the progress variable is defined to be zero in both the fuel and oxidizer streams [15].

In this work, both steady and unsteady flamelet equations are solved using a detailed chemistry mechanism including comprehensive PAH chemistry by Narayanaswamy *et al.* [85,86]. When creating the chemistry table, a presumed-PDF method [15,76,77] is employed to model subgrid-scale turbulence-chemistry interaction, in which the subgrid-scale mixture fraction distribution is assumed to be β-PDF distribution and δ-PDF is applied to the progress variable and enthalpy loss.

Given that soot particles are too numerous to track using a Lagrangian method individually, the soot population balance equation (PBE) is usually used to provide a theoretically accurate description of the soot number density function (NDF) [1]. Due to the high dimensionality of the NDF, it is impractical to solve it directly. In this context, a large number of early studies employed semi-empirical models [77,87,88]. Recently, statistical models such as the method of moments [12,15,89,90] and the sectional model [11,75,78,91] are widely used to address the high-dimensionality of the NDF. Here, the state-of-the-art hybrid method of moments (HMOM) approach, which is proposed by Mueller *et al.* [15,92,93], is employed to describe the evolution of soot particles. In HMOM, two internal coordinates volume (V) and surface (S) are used to describe the morphology of particle aggregates, leading to the moments of the NDF of order x and y in volume and surface area, respectively, being $M_{x,y} = \int V^x A^y N dV dA$ where N, V, A are the soot paritcle NDF, volume, and surface area, respectively. The unknown moments are obtained by interpolating the known moments using $M_{x,y} = N_0 V_0^x S_0^y + \exp(\sum_{r=0}^{R} \sum_{k=0}^{r} a_{r,k} x^k y^{r-k})$. $N_0 V_0^x S_0^y$ is a δ function fixed in state space (i.e., fixed V_0 and S_0) with N_0 being the function weight. $a_{r,k}$ is an interpolating coefficient calculated from the known moments. To reduce the computational expense, a first-order (R = 1) polynomial interpolation is considered. In this context, three moment transport equations are solved to describe the soot population: the total number density $M_{0,0}$, the total soot volume $M_{1,0}$, and the total soot surface area $M_{0,1}$. In addition, a transport equation of N_0 is solved. The corresponding transport equations of the bivariate soot particle moments can be derived from the PBE, and the filtered moment equations are given by

$$\frac{\partial \overline{M_{x,y}}}{\partial t} + \frac{\partial}{\partial x_j}(\widetilde{u_i}\overline{M_{x,y}}) = \frac{\partial}{\partial x_j}(\widetilde{u_i}\overline{M_{x,y}} - \overline{u_i M_{x,y}}) + \overline{\dot{M}}_{x,y}, \tag{9}$$

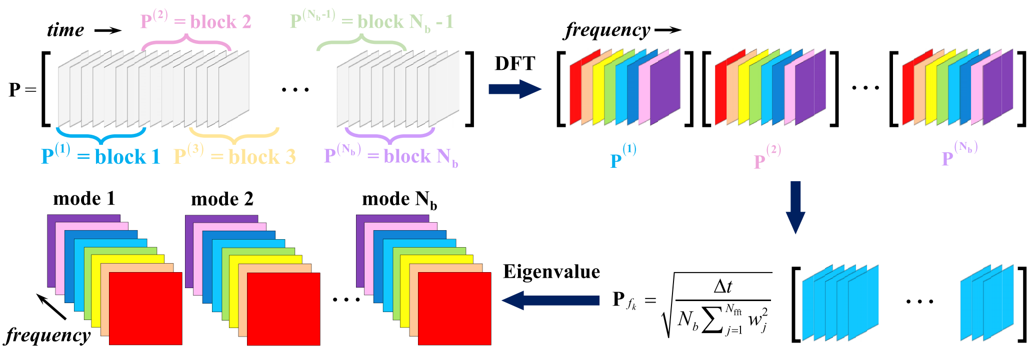

FIG. 4. Schematic depiction of Welch's method for estimating SPOD modes.

where $\dot{M}_{x,y}$ is the source term which consists of several subterms including PAH-based nucleation, PAH condensation, coagulation, oxidation, and surface growth via H-abstraction and C_2H_2 addition (HACA) mechanism [94]. The thermophoresis process is typically neglected for soot modeling [12,14]. Owing to the high Schmidt number of soot particles, the molecular diffusion term can also be neglected. The density of soot particles is 1800 $\mathrm{kg/m^3}$. Due to the large spatial intermittency of soot, the soot subfilter PDF is modeled by a double δ distribution [95]. Due to the large spatial intermittency of soot, the soot subfilter PDF is modeled by a double δ distribution [95]. While this subfilter PDF model for soot–turbulence interaction is known to have limitations in quantitative soot prediction, it can capture the strong spatial intermittency of soot through distinct sooting and nonsooting modes. Investigation of soot subfilter PDF is beyond the scope of this work. For more details on the HMOM model and the soot subfilter PDF, readers are referred to Ref. [15,92,93].

The Euler implicit method is used for the time integration of the governing equations, and a Gauss linear scheme is adopted for the evaluation of the convection terms. The PIMPLE method [96] is employed to address the pressure-velocity coupling involving two inner iterations and three outer iterations. The above modeling framework is implemented into a low-Mach number solver [10], which features the minimized dissipation of kinetic energy. The accuracy of the relevant computational models has been validated in our latest published paper [82]. The computational domain consists of approximately 12 M tetrahedral cells. A mesh sensitivity evaluation has been carefully performed by examining three meshes with sizes of 6, 12, and 77 million. It is found that the current mesh yields reasonable predictions for quantities of interest. Furthermore, the grid is refined near the wall with $y^+ < 0.7$ for the first layer and $6 \sim 7$ layers within $y^+ < 10$ to resolve the near-wall flow dynamics, where y^+ represents the wall coordinate.

III. SPOD METHOD

In this work, the SPOD technique is employed to identify coherent structures in the DLR combustor. The advantage of SPOD over conventional POD is that the time-domain oscillation of each mode identified at a separate frequency can be obtained [38,66]. Furthermore, the coherent structures identified by the SPOD method can characterize the space-time flow statistics in second-order accuracy [38,66].

While the cross-spectral density tensor can be estimated using the discrete Fourier transform of the nonblock data matrix, spectral estimation does not converge as the number of snapshots increases for the nonblock SPOD. To obtain a convergent estimate of the spectral densities, it is necessary to appropriately average the spectra over multiple realizations of the flow, i.e., block SPOD [38]. In this work, Welch's method [97] is used for estimating SPOD modes, which is shown in Fig. 4. The implementation of the SPOD method is briefly described below, and more details can be found in Towne *et al.* [38]. As shown in Fig. 4, for N_b data blocks, we consider the nth block, $\mathbf{P}^{(n)}$, which consists of N_{fft} snapshots. The block is then partitioned into smaller, overlapping subblocks,

$$\mathbf{P}^{(n)} = \left[\mathbf{p}_1^{(n)}, \mathbf{p}_2^{(n)}, \cdots, \mathbf{p}_{N_{\text{fft}}}^{(n)}\right], \tag{10}$$

where $\mathbf{p}_k^{(n)} = \mathbf{p}_{k+(n-1)(N_{\text{fft}}-N_{\text{ovlp}})}$ and $n = 1, 2, 3, \ \ldots, N_b$. N_{ovlp} is the number of snapshots over which the two blocks overlap.

Then, a windowed fast Fourier transform is used for the nth block,

$$\widehat{\mathbf{P}}^{(n)} = \text{FFT}(\mathbf{P}^{(n)}) = \left[\widehat{\mathbf{p}}_1^{(n)}, \widehat{\mathbf{p}}_2^{(n)}, \cdots, \widehat{\mathbf{p}}_{N_{\text{fft}}}^{(n)}\right]. \tag{11}$$

For each frequency $k = 1, 2, \ \ldots, N_{\text{fft}}$, the following steps are performed.

(1) Arrange the Fourier coefficients at the frequency of f_k from each block into the new data matrix:

$$\widehat{\mathbf{P}}_{f_k} = \sqrt{\frac{\Delta t}{N_b \sum_{j=1}^{N_{\text{fft}}} w_j^2}} \left[\widehat{\mathbf{p}}_k^{(1)}, \widehat{\mathbf{p}}_k^{(2)}, \cdots, \widehat{\mathbf{p}}_k^{(N_b)}\right], \tag{12}$$

(2) Calculate the matrix:

$$\mathbf{C}_{f_k} = \widehat{\mathbf{P}}_{f_k}^H \mathbf{W} \widehat{\mathbf{P}}_{f_k}, \tag{13}$$

(3) Reduce to an $N_b \times N_b$ matrix eigenvalue problem:

$$\mathbf{C}_{f_k} \mathbf{\Pi}_{f_k} = \mathbf{\Pi}_{f_k} \mathbf{\Lambda}_{f_k}, \tag{14}$$

(4) Obtain the SPOD modes:

$$\mathbf{\Phi}_{f_k} = \widehat{\mathbf{P}}_{f_k} \mathbf{\Pi}_{f_k} \mathbf{\Lambda}_{f_k}^{-1/2}, \tag{15}$$

where $\mathbf{\Lambda}_{f_k}$ denotes the modal energy of the kth frequency. The modes are sorted in descending order of modal energy, i.e., $\lambda_{f_k}^1 \geqslant \lambda_{f_k}^2 \geqslant \cdots \geqslant \lambda_{f_k}^{N_b}$.

The open-source Python package PySPOD [98] is used to perform the above SPOD using a time series of LES data, which are extracted from a central cross-section of the combustor, including axial velocity, PAH mass fraction, and soot volume fraction. The LES data with a physical duration of 200 ms are collected for the SPOD analysis presented in this work. Within the analyzed window, the statistical convergence of the sampled data is assessed using representative probe signals for temperature and integrated soot volume throughout the combustor. The quantitative analysis confirms that the sampled signals are statistically converged over the SPOD window, although slow long-time drifts can still be observed in some temperature probe signals. These drifts are minimal within the analyzed window and are not expected to affect the main results. The LES data for SPOD consists of 1001 snapshots, with a sampling frequency of 5000 Hz with an interval of 0.2 ms. A total sampling time is 200 ms, which is sufficient for spectral analysis of the combustor [10,11]. The parameters are set to $N_{\text{fft}} = 64$, $N_{\text{ovlp}} = 32$, $N_b = 30$.

IV. RESULTS AND DISCUSSION

In this section, the flow field is first analyzed, followed by comparisons of simulation results with experimental data to validate the models. Subsequently, SPOD is used to identify LFD and HFD in the combustor. Finally, the influence of flow dynamics on soot evolution is discussed for cases with and without dilution jets.

A. Characteristics of swirling flow

Figure 5 shows a representative snapshot of the flow field obtained from LES, in which the 2D streamlines (blue lines) are plotted to reveal the vortex near the inner shear layer. As indicated by the yellow arrows, the vortex exhibits a zigzag distribution, implying the presence of a 3D helical vortex

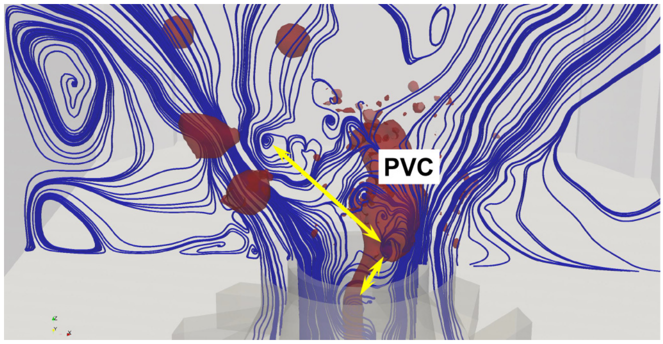

FIG. 5. Instantaneous flow field on a cross section, in which streamlines (blue) and isosurfaces of pressure (red) are included.

which is commonly termed PVC in the flow field [19]. The isosurface of pressure (red) in Fig. 5 indicates the vortex core generated within the swirling inflow, which breaks down at the nozzle and forms the PVC.

To further understand the swirling flow characteristics, the flow fields in the dual swirl combustor are shown in Fig. 6 for cases without and with dilution jets, in which the blue solid lines represent the zero axial velocity and the color bar represents the magnitude of the axial velocity.

To capture vortex structures, the streamlines are drawn densely in Fig. 6 where the zigzag vortex distribution is indicated by black arrows. It is seen from Fig. 6 that the time-averaged flow field contains three characteristic zones, i.e., IRZ, ORZ, and shear layer. In swirling flames, the IRZ plays an important role in flame stabilization by mixing hot combustion products with fresh reactants.

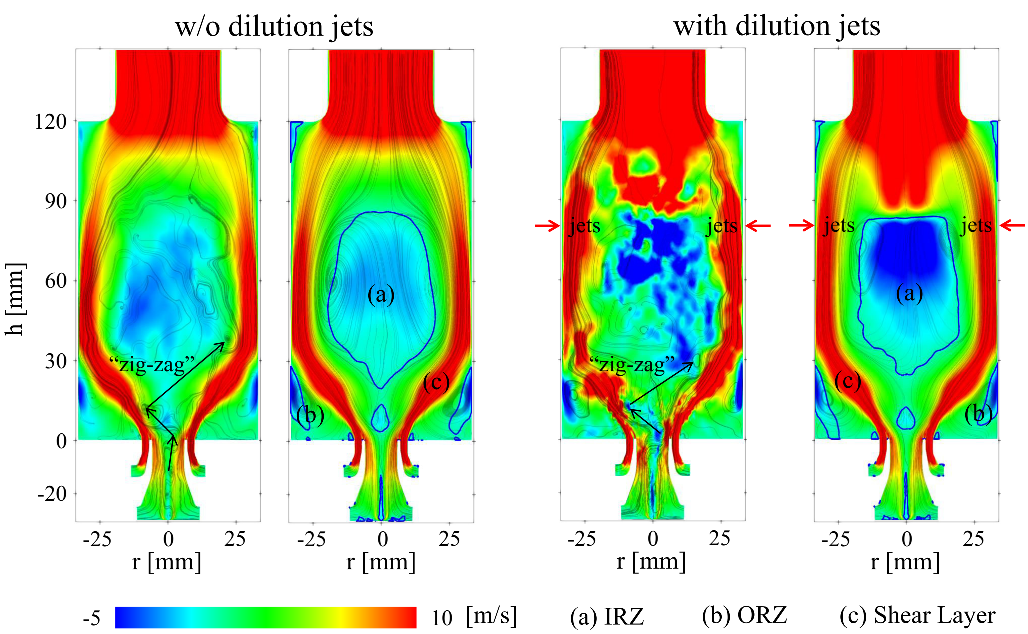

FIG. 6. Instantaneous and time-averaged axial velocity contours for cases without (left) and with (right) dilution jets. The instantaneous streamlines show the presence of PVC with a zigzag distribution. The three zones in the time-averaged figure represent IRZ, ORZ, and the shear layer, respectively, and the blue solid lines in the time-averaged figure represent zero axial velocity.

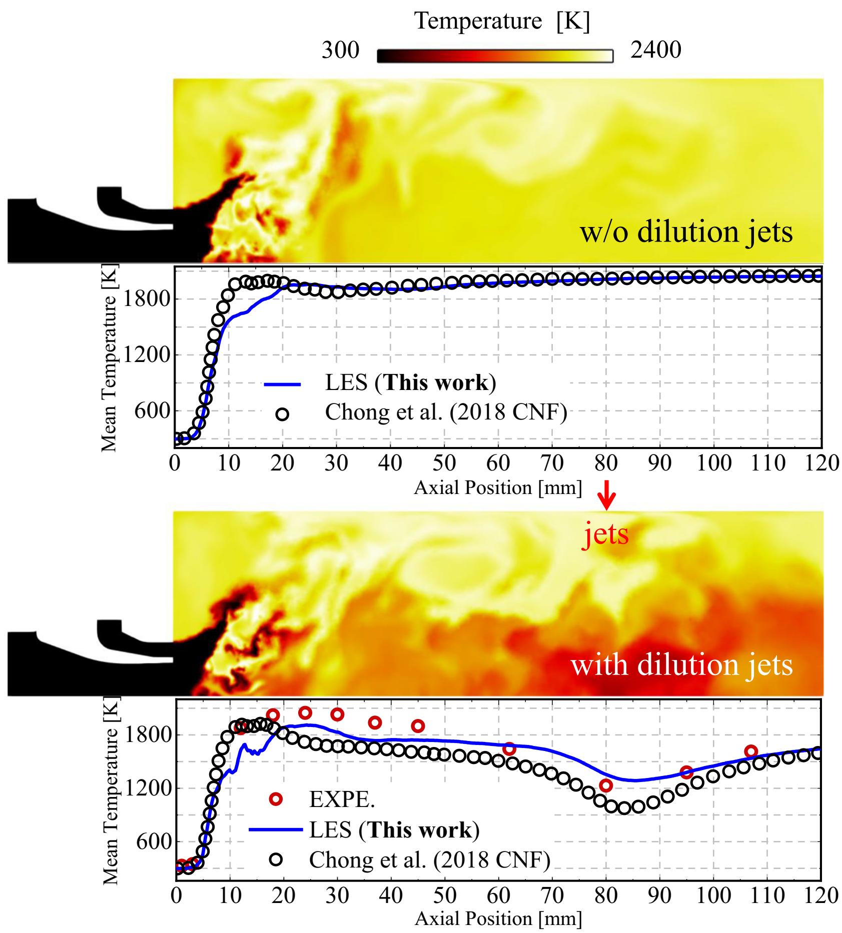

FIG. 7. Instantaneous temperature contours and the comparisons of time-averaged temperature between LES and experimental data from Ref. [7] for cases without (top) and with (bottom) dilution jets. The results from Ref. [12] have been included for comparison.

Furthermore, from the streamline of the time-averaged flow field, it can be observed that ORZs are present in the four right-angled edge regions of the combustor. The IRZ and ORZ are separated by a high-speed hollow cone, called the shear layer.

Comparing these two operating conditions shows that dilution jet injection can produce a more negative axial velocity in the IRZ, leading to stronger interaction with the upstream flow. Simultaneously, it reduces the local equivalence ratio, thereby accelerating soot oxidation and fragmentation and decreasing soot content. It is noted that the injection of dilution jets has a significant impact on IRZ, while having a negligible impact on the distributions of ORZ and the shear layer.

B. Comparisons between LES and experiment

Figure 7 shows the instantaneous temperature contour and compares the time-averaged temperature at the centerline between LES and experimental data, for without and with dilution jet cases. It is noted that the experimental data are not available for the case without dilution jets. It is observed that, under both operating conditions, the temperature peak is near the nozzle. In the case without dilution jets, the temperature approaches its peak and then changes slightly downstream. When introducing dilution jets, a distinct low-temperature zone forms downstream, with a significant

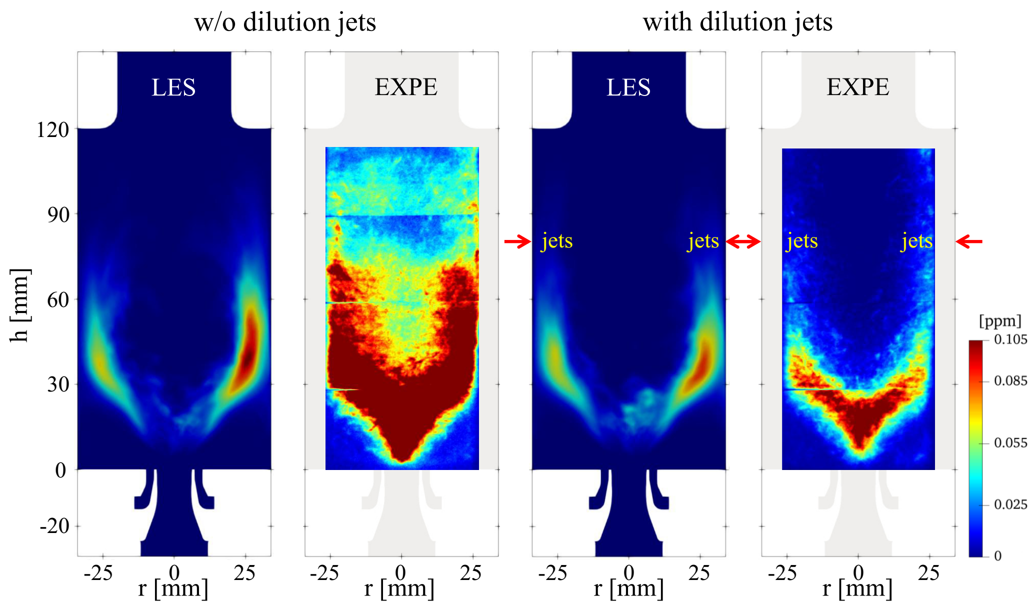

FIG. 8. Comparisons of time-averaged soot volume fraction between LES and experimental data from Ref. [7] for cases without and with dilution jets.

radial temperature gradient at the edge of the IRZ. This temperature gradient is also observed upstream and extends to the combustor exit. The dilution jets not only transport downstream but also play a role upstream, as indicated by the IRZ. Figure 7 indicates that the LES framework can accurately capture the temperature decrease in the IRZ.

The comparisons between LES results and experimental data for the time-averaged contours of soot volume fraction (SVF), f_V, are shown in Fig. 8. It is seen that LES can qualitatively capture the spatial distribution of SVF, especially in the case of dilution jets. The peak values of SVF are under-predicted by LES for both cases, especially near the nozzle and the IRZ. Figure 8 indicates that the soot emission is reduced due to the injection of dilution jets.

Moreover, Fig. 9 shows a detailed quantitative comparison between LES and experiments at three different axial positions ($h = 20$ mm, 45 mm, 80 mm) for the SVF statistics. Similar to the results from Chong *et al.* [12], it is found that the LES results differ from the experimental data by a factor of almost four.

It is noted that the state-of-the-art soot models still involve significant uncertainties. Nevertheless, Figs. 7–9 indicate that all relevant characteristics of soot formation for the two cases are covered by the current approach. In this context, although soot evolution is not entirely accurately predicted, an analysis restricted to flow dynamics is still possible, as suggested by Ref. [75].

C. Identification of low/high-frequency dynamics

The discussion of SPOD results begins with energy analysis. As mentioned above, the magnitude of eigenvalues in modal analysis represents the corresponding modal energy level. The energy summed over frequencies is examined to explore the contribution of energy within specific frequency bands to the total energy. Figure 10 shows the variation of $\xi(\text{freq})$ calculated as

$$\xi(\text{freq}) = \frac{\sum_{f=f_1}^{\text{freq}} \sum_{i=1}^{N_b} \lambda_f^i}{\sum_{f=f_1}^{N_{\text{fft}}} \sum_{i=1}^{N_b} \lambda_f^i}. \tag{16}$$

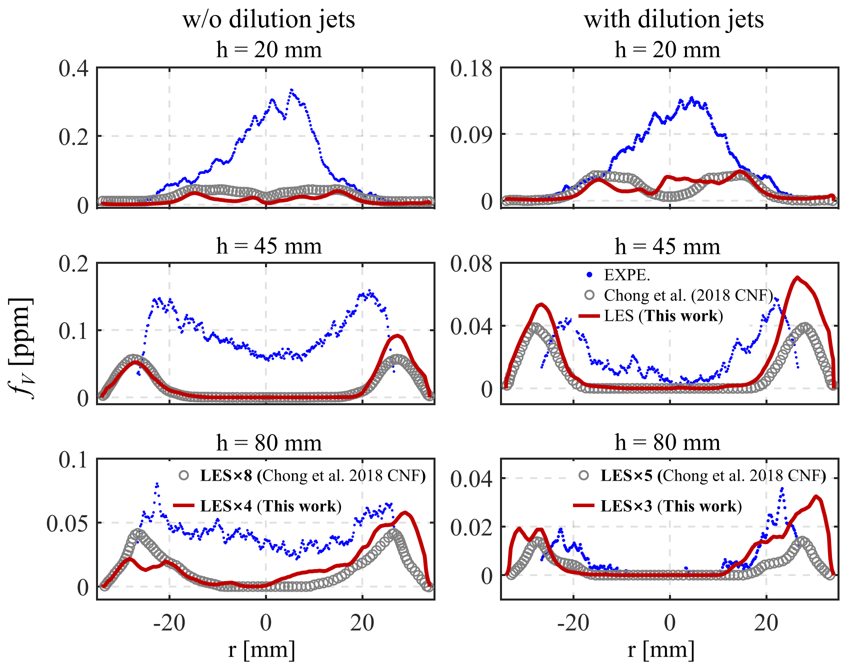

FIG. 9. Comparisons of soot volume fraction between LES (red lines) and experimental data (blue dots) at three axial locations for cases without and with dilution jets. The results from Ref. [12] have been included for comparison.

For the λ_f^i, i represents the number of modes and f represents the frequencies. Eq. (16) calculates the cumulative fraction of energy as a function of frequency by summarizing the modes first and the frequencies. Figure 10 shows the variation of the cumulative fraction of energy, $\xi(\text{freq})$, as a function of frequency for cases without and with dilution jets. It is found that $\xi(\text{freq})$ increases rapidly with increasing frequency, then the growth rate slows until it approaches 1.0 for both cases with and without dilution jets. Notably, there is a rapid accumulation of energy in the frequency

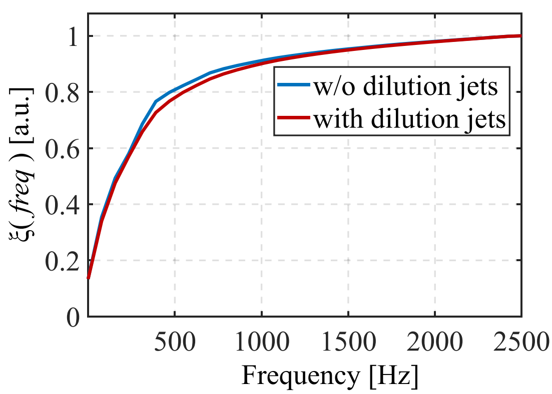

FIG. 10. Variation of the cumulative fraction of energy, $\xi(\text{freq})$, as a fraction of frequency for cases without and with dilution jets.

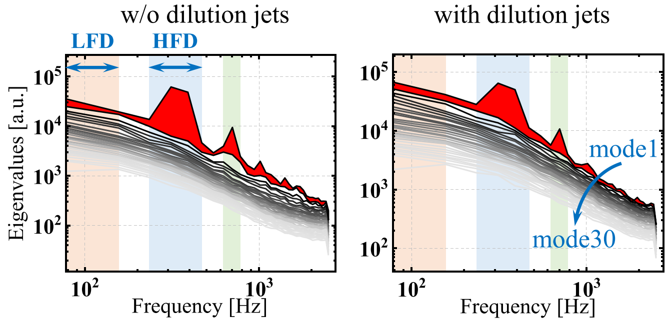

FIG. 11. SPOD eigenvalue spectra of axial velocity (U) for cases without and with dilution jets. Blue-shaded areas represent the PVC frequency band, and green areas represent the second harmonic of PVC. The red-shaded areas highlight the differences between the first and second modes and can characterize the energy contribution of the leading mode. The frequency bands for LFD and HFD (or PVC) are marked in orange and blue, respectively.

band below 500 Hz, accounting for about 80% of the total energy in both cases. This indicates the presence of one or more high-energy dynamic structures in the combustor below 500 Hz.

To identify the leading mode and corresponding frequency band in the combustor, the SPOD eigenvalue spectra of axial velocity (U) for cases without and with dilution jets are shown in Fig. 11. The red-shaded areas highlight the differences between the first and second modes. A large difference indicates that the leading (first) mode is effectively more energetic than the rest, which is referred to as "low-rank behavior" within a certain frequency band. In this context, it is seen from Fig. 11 that U exhibits low-rank behavior within two frequency bands, which are marked by the blue and green shades, respectively.

It is well known that PVC is the most energetic motion in swirling flows [11,19], and its structure is found to have the second or even higher-order harmonics, while the first harmonic always dominates [19]. Figure 11 demonstrates that the flow field exhibits prominent low-rank behavior within the frequency band of [234.375, 468.75] Hz with the middle frequency of 351.5625 Hz for both cases. In this sense, the frequency band marked by blue shade is supposed to be the first harmonic of PVC, and the frequency band of [625, 781.25] Hz with the middle frequency of 703.125 Hz marked by green shade should represent its second harmonic, since 351.5625 Hz and 703.125 Hz have a 1:2 frequency ratio. Given the dominant role of the first harmonic of PVC, the low-rank behavior in [234.375, 468.75] Hz is denoted as HFD. It is observed that the introduction of dilution jets can weaken low-rank behavior, i.e., reduce the area of the red shade, and thus decrease the dominance of the leading mode. Moreover, Fig. 11 shows that the differences between the first and second modes vanish toward higher frequencies while maintaining a certain value when toward lower ones, which suggests that the low-rank behavior also exists within the low-frequency range of [0, 156.25] Hz marked by the orange shade, which represents LFD.

To better identify LFD, the energy of axial velocity (U) accounted by each SPOD mode as a function of frequency for cases without and with dilution jets is shown in Fig. 12. Similarly, blue boxes represent the PVC frequency band, and the green boxes are the second harmonic of PVC. The LFD frequency bands are marked with orange boxes in both cases. It is observed that in both cases, LFD and HFD exhibit a significant energy contribution from the leading mode within their corresponding frequency band, while showing a slight energy contribution from the second harmonic frequency band of HFD. The energy contribution of LFD is particularly evident in dilution jets, as their injection weakens the dominant role of HFD. The frequency bands of the two high-energy dynamic coherent structures are below 500 Hz, corresponding to the fast energy accumulation process in Fig. 10.

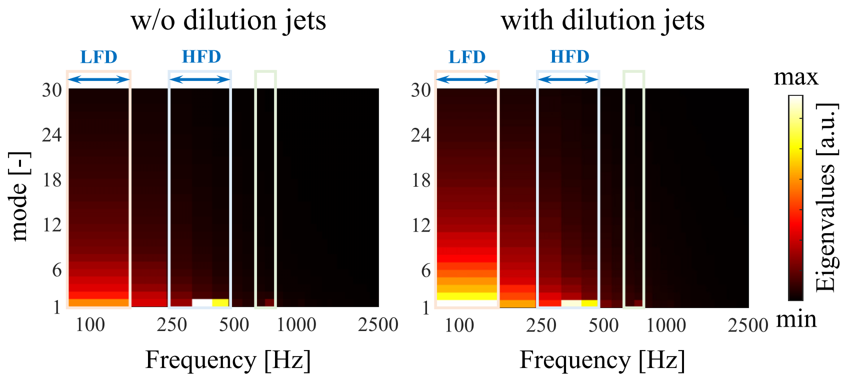

FIG. 12. Energy contours of axial velocity (U) accounted by each SPOD mode as a function of frequency for cases without and with dilution jets. Blue boxes represent the PVC frequency band, and the green boxes are the second harmonic of PVC. The LFD frequency bands are marked with orange boxes in both cases.

D. Impact of high-frequency dynamics on soot

In this section, the impact of LFD and HFD identified above on soot formation and evolution will be examined. To this end, the SPOD analysis for PAH mass fraction (Y_{PAH}) and SVF (f_V) are performed, and their eigenvalue spectra are shown in Fig. 13. The shade areas are consistent with those in Fig. 11. It can be seen that the eigenvalue spectra of Y_{PAH} and f_V exhibit significant low-rank behavior within the HFD frequency band, indicating that HFD has a significant impact on the evolution of Y_{PAH} and f_V. It is worth mentioning that Y_{PAH} exhibits low-rank behavior in the

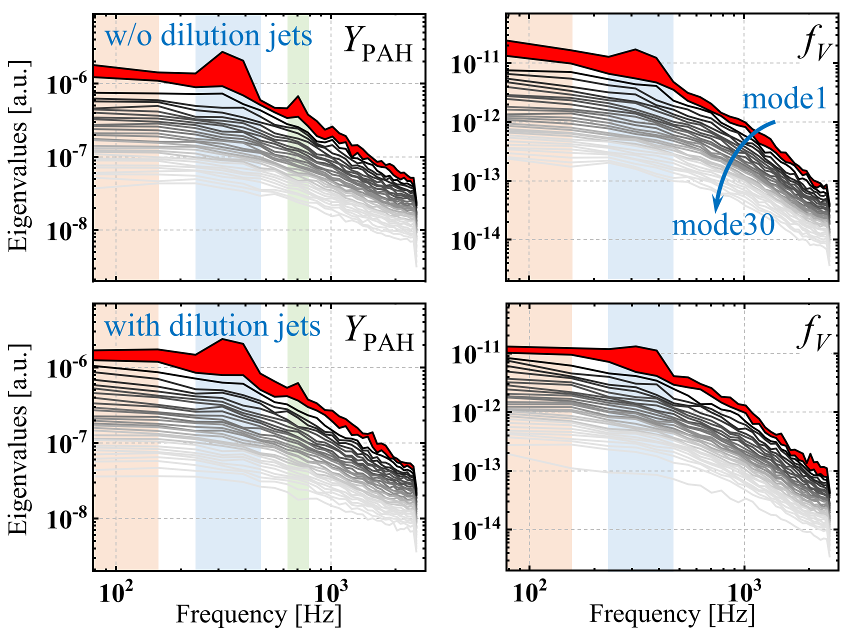

FIG. 13. SPOD eigenvalue spectra of PAH mass fraction (Y_{PAH}), and soot volume fraction (f_V) for cases without (top) and with (bottom) dilution jets. Blue-shaded areas represent the PVC frequency band, and green areas represent the second harmonic of PVC. Red shaded areas highlight the differences between the first and second modes. The frequency bands for LFD and HFD (or PVC) are marked in orange and blue, respectively.

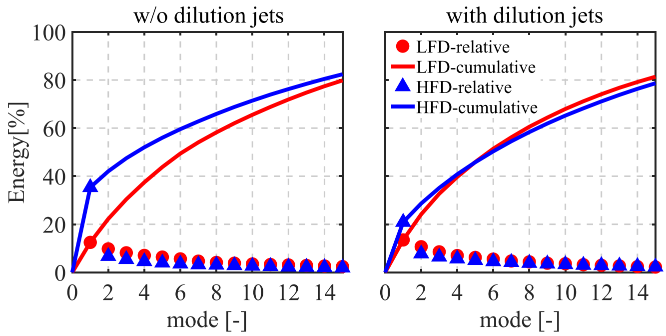

FIG. 14. Energy contributions of the respective modes of U within the LFD and HFD frequency bands.

second harmonic frequency band of HFD, while f_V is not affected by it and only shows low-rank behavior in the HFD frequency band.

Both relative and cumulative energy contributions of each SPOD mode of U are demonstrated in Fig. 14 for cases with and without dilution jets. For HFD (blue lines and symbols), the first mode plays a leading role with the contribution of 40% for the case without dilution jets, while for the dilution case, the first mode only contributes to 20% of SPOD energy due to the impact of dilution jets on HFD, which is consistent with the low-rank behavior observed in Fig. 11. In a review paper on the role of PVC in swirling flows, Ref. [19] mentioned that the equivalence ratio is a key factor affecting the energy of PVC. It has been shown that strong helical coherent structures can form when the equivalence ratio exceeds a certain value. The injection of dilution jets reduces the global equivalence ratio, thereby suppressing HFD energy. For LFD (red lines and symbols), the modal energy is evenly distributed among different modes, and dilution jets have a negligible impact on modal energy.

The injection of dilution jets weakens the dominant role of HFD in the flow field and has a negligible impact on LFD. To further examine the impact of dilution jets on the evolution of PAH and SVF, relative energy contributions of each SPOD mode of Y_{PAH} and f_V are analyzed (see Fig. 19) for cases with and without dilution jets. It can be seen that dilution jets can reduce the energy contribution of the leading mode of LFD for the SVF field, whereas the gas-phase PAH remains unaffected within the HFD and LFD frequency bands.

It is seen from Figs. 11 and 13 that for HFD, the differences between the first and second modes are gradually narrowed from U to f_V, which indicates the low-rank behaviors gradually become less apparent. Moreover, the second harmonic of HFD gradually becomes less prominent, and the f_V does not even exhibit low-rank behavior in the second harmonic frequency band (green shaded area in Figs. 11 and 13). This indicates that from U to f_V, the dominant role of HFD and its second harmonic gradually weakens, while other coherent structures affect the evolution of PAH and SVF.

Furthermore, the time-averaged axial velocity contours and the leading mode at characteristic frequencies are shown in Fig. 15. In the figure, the solid blue lines represent the zero axial velocity. LFD are characterized by slow time-scale coherent structures in recirculation zones, while HFD are characterized by fast time-scale coherent structures in the shear layers. The injection of dilution jets introduces coherent structures at both slow and fast timescales near the IRZ, indicating that low- and high-frequency velocity perturbations coexist in this zone. The HFD mode exhibits a typical helical structure, with local maxima and minima arranged in a “zigzag” distribution along the shear layer. Compared with the LFD, the time-averaged velocity contours are highly similar to the HFD mode shapes, confirming that the HFD represents the most energetic coherent structure. It is noted that the frequencies of 312.5 Hz (blue shaded band in Fig. 11) and 703.125 Hz (green shaded band in Fig. 11) have a harmonic relationship, and the physical distribution of coherent structures at these two frequencies follows the same pattern. This indicates that the physical mechanisms associated

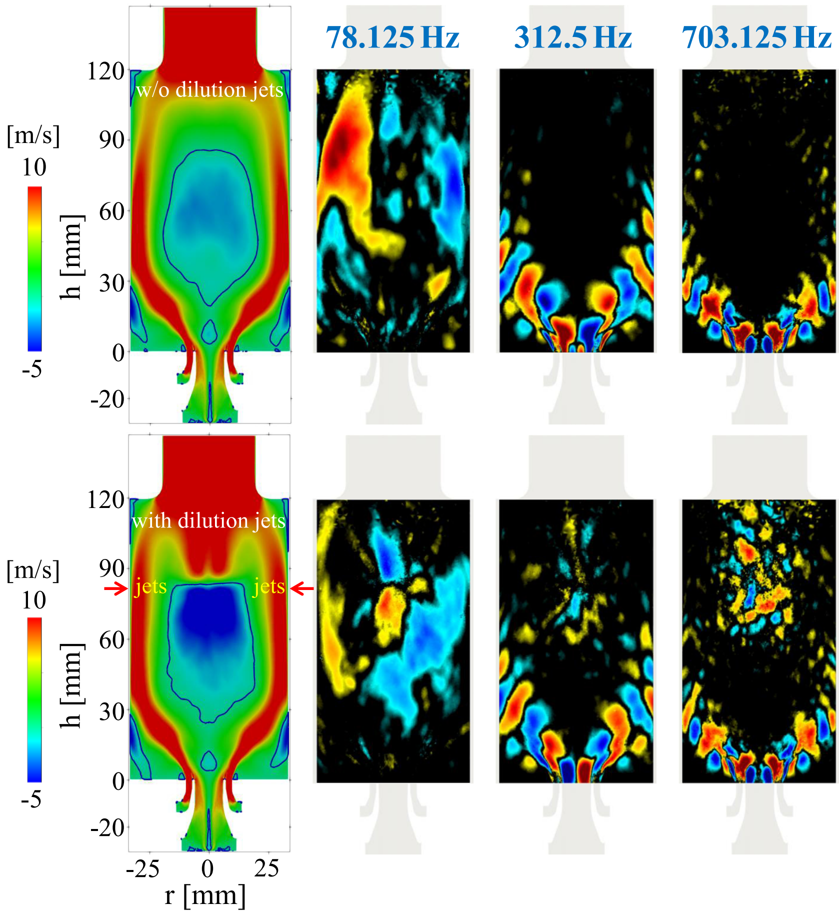

FIG. 15. Time-averaged contours of U and the leading modes at three characteristic frequencies for cases without (top) and with (bottom) dilution jets. The blue solid lines in the left contours represent the zero axial velocity.

with mode formation at both frequencies are consistent, suggesting that the two frequency bands correspond to the PVC and its second harmonic, respectively.

E. Impact of low-frequency dynamics on soot

Figure 16 shows the temporal signal of integrated SVF and its fast Fourier transformation (FFT) for the dilution case. It is seen that soot evolution is a low-frequency, high-intermittency process. The case without dilution jets exhibits similar dynamics (not shown here). Based on the previous discussion, the SVF exhibits a certain low-rank behavior in the HFD frequency band, indicating an influence by HFD. However, the question is whether this low-frequency evolution process is coupled with the LFD. In this context, it is necessary to explore the impact of LFD on soot formation and evolution.

For this purpose, Fig. 17 shows the time-averaged contours of Y_{PAH} and f_V for cases without and with dilution jets, as well as the shapes of the leading mode at certain characteristic frequencies in the LFD and HFD (orange and blue shades in Fig. 13). For PAH, both LFD and HFD are present in the shear layers due to the slow PAH formation chemistry and the dependence of PAH on fuel oxidation. In this sense, LFD can affect soot formation by influencing PAH.

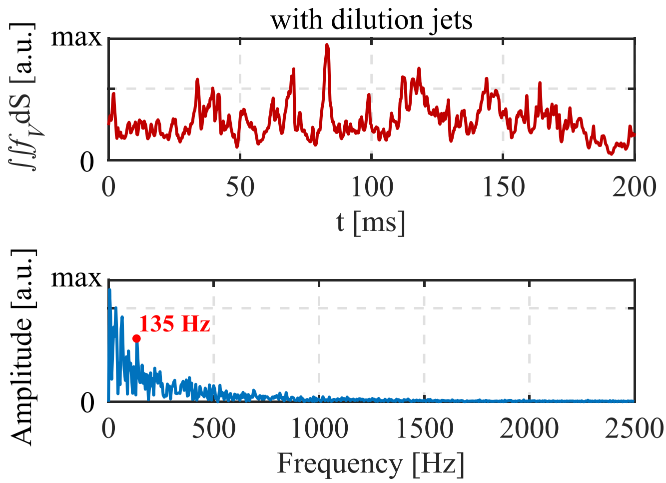

FIG. 16. Evolution of integrated soot volume fraction and its FFT.

For the case with dilution jets, coherent structures appear near the nozzle region in the LFD modes of both PAH and soot, as highlighted by the white circles. This behavior can be attributed to the negative axial velocity in the IRZ, which entrains the injected dilution jets upstream toward the

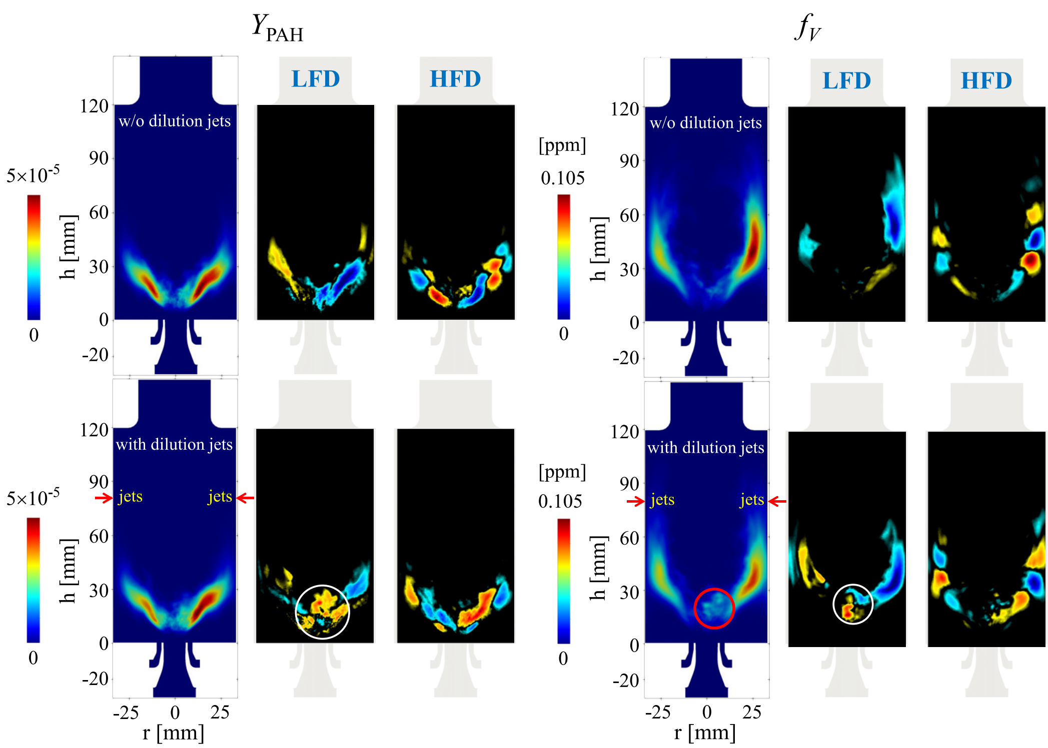

FIG. 17. Time-averaged contours and the leading mode distributions of Y_{PAH} (left) and f_V (right) at the frequency of 78.125 Hz for LFD and the frequency of 312.5 Hz for HFD in cases without and with dilution jets.

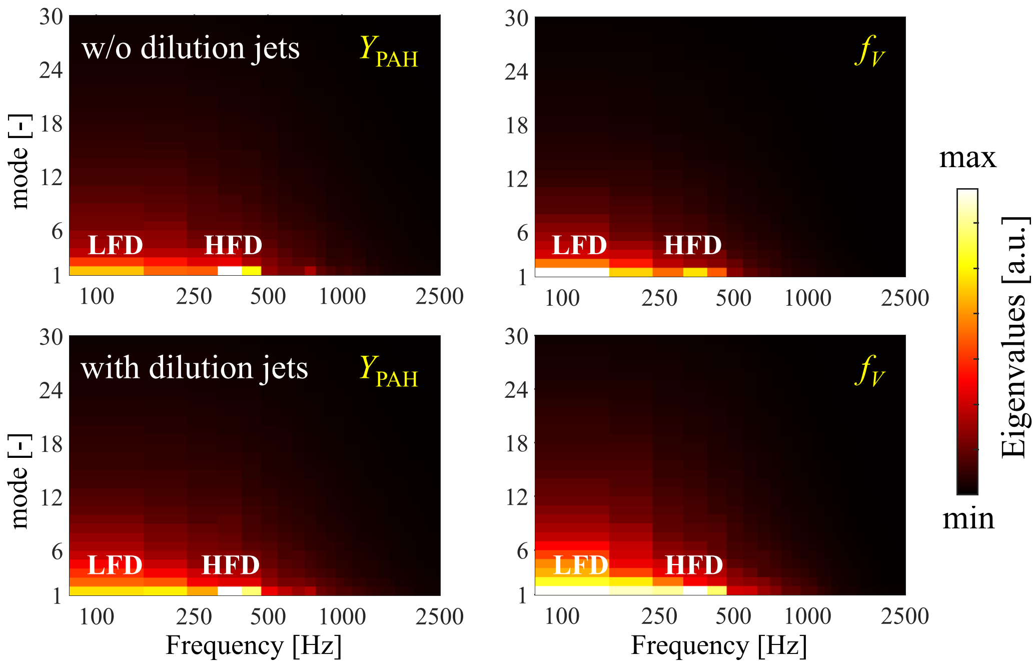

FIG. 18. Energy contours of PAH mass fraction (Y_{PAH}) and soot volume fraction (f_V) accounted by each SPOD mode as a function of frequency for cases without (top) and with (bottom) dilution jets.

nozzle region. The characteristic timescale for the dilution jets to travel from the injection location ($h = 80$ mm) to the vicinity of the nozzle ($h \approx 20$ mm) is comparable to that of the LFD, leading to the emergence of this structure in the LFD modes of both quantities.

A stronger resemblance between a SPOD mode shape and the time-averaged contour generally indicates a stronger response of that quantity to the corresponding frequency band. For soot, the LFD mode shows high similarity to the time-averaged contour of f_V, especially in capturing the coherent structure near the nozzle for the case with dilution jets, as indicated by the red and white circles in the right of Fig. 17. For PAH, a localized lob near the nozzle attached to the right shear layer is also visible in the time-averaged field. However, this feature is spatially limited and more closely resembles the HFD mode than the broader coherent structure observed in the LFD mode. This is consistent with the earlier observation that the PAH eigenvalue spectra in the HFD and the harmonic frequency bands exhibit significant low-rank behavior, suggesting that HFD has a greater impact on PAH evolution than LFD. Therefore, from the perspective of spatial mode distribution, PAH evolution is more strongly influenced by HFD, whereas soot evolution is more strongly governed by LFD.

To further confirm the sensitivities of PAH and SVF to the two dynamic structures, the energy contours from the cases without and with dilution jets are shown in Fig. 18, in which the sensitivity of these two physical quantities to the two dynamic structures is compared from the perspective of mode energy. It is seen that for gas-phase PAH, the HFD energy is more dominant than the LFD. Meanwhile, SVF is affected by both the HFD and LFD. Nevertheless, LFD plays a more important role than HFD, whether or not the dilution jets are injected. The above findings are consistent with the results from Fig. 17.

Besides, the sensitivities of SVF and PAH to LFD and HFD are further quantitatively examined in Fig. 19. It is found that for the leading mode, PAH is more susceptible to HFD than LFD, while the opposite trend is observed for SVF. These findings are consistent with the results in Ref. [11]. Moreover, Fig. 19 shows that introducing dilution jets would mitigate the difference in

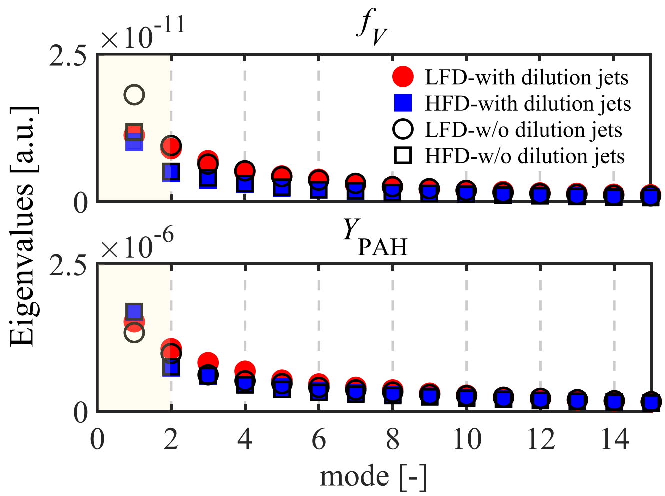

FIG. 19. Energy of the respective modes for f_V (top) and Y_{PAH} (bottom).

sensitivities of SVF to LFD and HFD, while the LFD still slightly dominates over HFD. In summary, the sensitivities of gas-phase PAH and low-frequency SVF to the coherent structures of LFD and HFD in the flow field are analyzed using mode distribution and mode energy, respectively, yielding consistent conclusions.

F. Discussion

In the present work, no model-specific assumptions are imposed on the SPOD analysis regarding coherent structures or their characteristic frequencies. Instead, the dominant modes are extracted directly from the raw LES data without any *a priori* filtering. This is particularly important for sooting swirl flames, where turbulent-chemistry-soot interactions are highly intermittent and characteristic frequencies are not known in advance. In contrast to previous studies that relied on predefined band-pass filtering to isolate specific dynamics [11], the present work provides an objective modal decomposition of velocity, PAH, and soot within a unified framework.

The above results indicate a clear scale-dependent separation between PAH and soot evolution in the combustor. Although the chemical timescale of PAH is relatively slow, its evolution is more readily influenced by energetic HFD. This behavior is distinct from that of soot particles, whose evolution is more strongly associated with LFD. Although this behavior should not be interpreted as universally valid for all configurations, it shows that gas-phase precursors and soot particles do not necessarily respond to the same coherent structures, even when they remain chemically and dynamically coupled.

Furthermore, the injection of dilution jets modifies the global equivalence ratio and weakens the energetic contribution of HFD in the flow field. Since the characteristic timescale of the dilution jets is comparable to that of the LFD, their effect is also manifested in the LFD mode shapes of both PAH and soot. In addition, the dilution jets reduce the sensitivity difference between PAH and soot to coherent structures. This comparison provides additional insight beyond Ref. [11] by quantifying how dilution jets modify the coupling among coherent structures, gas-phase precursors, and soot evolution.

Overall, the present work provides new insight into the scale-dependent dynamics of soot formation and evolution in the confined turbulent swirling combustor by systematically comparing the responses of flow, gas-phase PAH, and solid-phase soot particles to low- and high-frequency coherent structures. It is noted that the purpose of this work is not to propose a universal rule for all sooting flames, but to investigate how PAH and soot respond differently to coherent structures across frequency bands and how this behavior is modified by dilution jets under elevated-pressure conditions. While the specific physical conclusions remain tied to the present configuration, the analysis framework itself is expected to be applicable, to some extent, to other sooting swirl flames for identifying frequency-dependent soot-flow coupling.

V. CONCLUSIONS

In this study, state-of-the-art soot models are used to simulate two aeroengine combustors, with and without dilution jets. The coherent structures of sooting swirl flames in the combustors are extracted and analyzed using SPOD without adding any *prior* information. The impact of LFD and HFD on soot formation is investigated. To the best of the authors' knowledge, this work is the first to use SPOD and raw LES data to elucidate the dynamics of coherent structures in sooting swirl flames under elevated pressure. It is noted that the state-of-the-art soot models still involve significant uncertainties. Nevertheless, all relevant characteristics of soot formation for the two cases are covered by the current approach. In this context, although soot evolution is not entirely accurately predicted, an analysis restricted to flow dynamics is still possible, as suggested by Grader *et al.* [75].

It is found that injecting dilution jets produces a large region of negative axial velocity that affects the upstream region, with a propagation timescale similar to that of LFD. Moreover, the introduction of dilution jets enhances soot oxidation, significantly reducing the SVF. In both cases, with and without dilution jets, the variation of cumulative energy with frequency indicates the presence of one or more high-energy dynamic structures below 500 Hz. Furthermore, LFD and HFD are successfully identified without *a priori* filtering from the SPOD eigenvalue spectra and energy contours. The axial velocity exhibits low-rank behavior in both the HFD and its second-harmonic frequency bands for cases with and without dilution jets, i.e., the leading modes have significantly higher energy content than the other modes. Moreover, HFD is found to occur mainly within the shear layer and IRZ, whereas LFD is primarily present in the recirculation zones. The results show that PVC (or HFD) is the most energetic motion, as confirmed by the velocity eigenvalue spectra and mode shapes.

Subsequently, SPOD analysis is conducted on the PAH mass fraction (Y_{PAH}) and SVF (f_V). The obtained eigenvalue spectra exhibit significant low-rank behavior within the HFD frequency band, indicating that both can be affected by the HFD of flow fields. From U to Y_{PAH} and then to f_V, the low-rank behavior within the HFD frequency band gradually becomes less apparent, and the dominant dynamic characteristics of HFD are gradually weakened.

Furthermore, the effects of dilution jets on velocity and SVF fields are quantitatively analyzed. It is found that dilution jets would significantly reduce the energy contribution of the first HFD mode of U by 20% while having a negligible impact on the first LFD mode. The injection of dilution jets also reduces the first-mode energy of the SVF field within the HFD frequency band. However, dilution jets have a negligible effect on the mode energy of gas-phase PAH within both the HFD and LFD frequency bands.

The temporal evolution of integrated SVF is analyzed using the FFT, revealing that soot evolution is a low-frequency process. Through qualitative comparison of the SPOD mode shapes between gas-phase PAH and solid soot particles, as well as quantitative comparison of the leading modes of both, it is found that PAH is more susceptible to HFD, while the opposite trend is observed for soot evolution, which is attributed to the influence of LFD on the soot evolution. Furthermore, the introduction of dilution jets can lead to the formation of significant coherent structures near the nozzle, associated with a large region of negative axial velocity induced by the jets.

ACKNOWLEDGMENTS

This work was supported by the National Natural Science Foundation of China (Grants No. 124B2045 and No. 52376090) and the National Key Research and Development Program of China (Grant No. 2022YFF0504500).

DATA AVAILABILITY

There are no publicly available research data or software supporting this manuscript. Requests for further information or data should be sent to the authors.

---

[1] V. Raman and R. Fox, Modeling of fine-particle formation in turbulent flames, Annu. Rev. Fluid Mech. **48**, 159 (2016).
[2] Y. Wang and S. Chung, Soot formation in laminar counterflow flames, Prog. Energy Combust. Sci. **74**, 152 (2019).
[3] T. Bond, S. Doherty, D. Fahey, P. Forster, T. Berntsen, B. DeAngelo, M. Flanner, S. Ghan, B. Kärcher, D. Koch, *et al.*, Bounding the role of black carbon in the climate system: A scientific assessment, JGR Atmospheres **118**, 5380 (2013).
[4] J. Hansen and L. Nazarenko, Soot climate forcing via snow and ice albedos, Proc. Natl. Acad. Sci. USA **101**, 423 (2004).
[5] J. Schwartz and D. Dockery, Increased mortality in Philadelphia associated with daily air pollution concentrations, Am. Rev. Respir Dis. **145**, 600 (1992).
[6] J. Schwartz, F. Laden, and A. Zanobetti, The concentration-response relation between PM (2.5) and daily deaths., Environ Health Perspect **110**, 1025 (2002).
[7] K. Geigle, R. Hadef, M. Stöhr, and W. Meier, Flow field characterization of pressurized sooting swirl flames and relation to soot distributions, Proc. Combust. Inst. **36**, 3917 (2017).
[8] K. Geigle, R. Hadef, and W. Meier, Soot formation and flame characterization of an aero-engine model combustor burning ethylene at elevated pressure, J. Eng. Gas Turbines Power **136**, 021505 (2013).
[9] C. Eberle, P. Gerlinger, K. Geigle, and M. Aigner, Numerical investigation of transient soot evolution processes in an aero-engine model combustor, Combust. Sci. Technol. **187**, 1841 (2015).
[10] S. Chong, V. Raman, M. Mueller, and H. Im, The role of recirculation zones in soot formation in aircraft combustors, in *Turbo Expo: Power for Land, Sea, and Air*, Vol. 51067 (American Society of Mechanical Engineers, New York, NY, 2018), p. V04BT04A008.
[11] M. Grader, Z. Yin, K. Geigle, and P. Gerlinger, Influence of flow field dynamics on soot evolution in an aero-engine model combustor, Proc. Combust. Inst. **38**, 6421 (2021).
[12] S. Chong, M. Hassanaly, H. Koo, M. Mueller, V. Raman, and K. Geigle, Large eddy simulation of pressure and dilution-jet effects on soot formation in a model aircraft swirl combustor, Combust. Flame **192**, 452 (2018).
[13] H. Koo, M. Hassanaly, V. Raman, M. Mueller, and K. Geigle, Large-eddy simulation of soot formation in a model gas turbine combustor, J. Eng. Gas Turbines Power **139**, 031503 (2016).
[14] F. Bisetti, G. Blanquart, M. Mueller, and H. Pitsch, On the formation and early evolution of soot in turbulent nonpremixed flames, Combust. Flame **159**, 317 (2012).
[15] M. Mueller and H. Pitsch, LES model for sooting turbulent nonpremixed flames, Combust. Flame **159**, 2166 (2012).
[16] M. Stöhr, C. Arndt, and W. Meier, Effects of Damköhler number on vortex-flame interaction in a gas turbine model combustor, Proc. Combust. Inst. **34**, 3107 (2013).
[17] J. Zhang, X. Hui, Q. An, and A. Steinberg, Transient dynamics of the precessing vortex core in an intermittently shape-transitioning swirl flame, Combust. Flame **250**, 112652 (2023).
[18] S. Wang, J. Zheng, L. Xu, Q. An, X. Han, C. Zhang, L. Li, X. Xia, and F. Qi, Experimental investigation of the helical mode in a stratified swirling flame, Combust. Flame **244**, 112268 (2022).
[19] N. Syred, A review of oscillation mechanisms and the role of the precessing vortex core (PVC) in swirl combustion systems, Prog. Energy Combust. Sci. **32**, 93 (2006).
[20] M. Freitag, M. Klein, M. Gregor, D. Geyer, C. Schneider, A. Dreizler, and J. Janicka, Mixing analysis of a swirling recirculating flow using DNS and experimental data, Int. J. Heat Fluid Flow **27**, 636 (2006).

[21] J. Fröhlich, M. García-Villalba, and W. Rodi, Scalar mixing and large-scale coherent structures in a turbulent swirling jet, Flow, Turbul. Combust. **80**, 47 (2008).
[22] D. Galley, S. Ducruix, F. Lacas, and D. Veynante, Mixing and stabilization study of a partially premixed swirling flame using laser induced fluorescence, Combust. Flame **158**, 155 (2011).
[23] M. Stöhr, C. Arndt, and W. Meier, Transient effects of fuel-air mixing in a partially-premixed turbulent swirl flame, Proc. Combust. Inst. **35**, 3327 (2015).
[24] M. Stöhr, R. Sadanandan, and W. Meier, Phase-resolved characterization of vortex–flame interaction in a turbulent swirl flame, Exp. Fluids **51**, 1153 (2011).
[25] M. Stöhr, I. Boxx, C. Carter, and W. Meier, Experimental study of vortex-flame interaction in a gas turbine model combustor, Combust. Flame **159**, 2636 (2012).
[26] A. Steinberg, I. Boxx, M. Stöhr, C. Carter, and W. Meier, Flow–flame interactions causing acoustically coupled heat release fluctuations in a thermo-acoustically unstable gas turbine model combustor, Combust. Flame **157**, 2250 (2010).
[27] J. Moeck, J.-F. Bourgouin, D. Durox, T. Schuller, and S. Candel, Nonlinear interaction between a precessing vortex core and acoustic oscillations in a turbulent swirling flame, Combust. Flame **159**, 2650 (2012).
[28] J. O'Connor and T. Lieuwen, Recirculation zone dynamics of a transversely excited swirl flow and flame, Phys. Fluids **24**, 075107 (2012).
[29] H. Richter and J. Howard, Formation of polycyclic aromatic hydrocarbons and their growth to soot—A review of chemical reaction pathways, Prog. Energy Combust. Sci. **26**, 565 (2000).
[30] S. Nidhan, O. Schmidt, and S. Sarkar, Analysis of coherence in turbulent stratified wakes using spectral proper orthogonal decomposition, J. Fluid Mech. **934**, A12 (2022).
[31] K. Taira, M. Hemati, S. Brunton, Y. Sun, K. Duraisamy, S. Bagheri, S. Dawson, and C.-A. Yeh, Modal analysis of fluid flows: Applications and outlook, AIAA J. **58**, 998 (2020).
[32] C. Rowley and S. Dawson, Model reduction for flow analysis and control, Annu. Rev. Fluid Mech. **49**, 387 (2017).
[33] J. Lumley, The structure of inhomogeneous turbulent flows, in *Atmospheric Turbulence and Radio Wave Propagation*, edited by A. M. Yaglom and V. I. Tatarski (Nauka, Moscow, 1967), pp. 166–178.
[34] J. Lumley, *Stochastic Tools in Turbulence* (Academic Press, San Diego, CA, 1970).
[35] M. Sieber, C. Paschereit, and K. Oberleithner, Spectral proper orthogonal decomposition, J. Fluid Mech. **792**, 798 (2016).
[36] P. Schmid, Dynamic mode decomposition of numerical and experimental data, J. Fluid Mech. **656**, 5 (2010).
[37] M. Mendez, M. Balabane, and J.-M. Buchlin, Multi-scale proper orthogonal decomposition of complex fluid flows, J. Fluid Mech. **870**, 988 (2019).
[38] A. Towne, O. Schmidt, and T. Colonius, Spectral proper orthogonal decomposition and its relationship to dynamic mode decomposition and resolvent analysis, J. Fluid Mech. **847**, 821 (2018).
[39] I. Litvinov, J. Yoon, C. Noren, M. Stöhr, I. Boxx, and K. Geigle, Time-resolved study of mixing and reaction in an aero-engine model combustor at increased pressure, Combust. Flame **231**, 111474 (2021).
[40] L. Abreu, A. Cavalieri, P. Schlatter, R. Vinuesa, and D. Henningson, Spectral proper orthogonal decomposition and resolvent analysis of near-wall coherent structures in turbulent pipe flows, J. Fluid Mech. **900**, A11 (2020).
[41] L. Abreu, A. Cavalieri, and W. Wolf, Coherent hydrodynamic waves and trailing-edge noise, in *Proceedings of the 23rd AIAA/CEAS Aeroacoustics Conference* (AIAA, Inc., Denver, Colorado, 2017), p. 3173.
[42] N. Rosafio, G. De Cosmo, S. Salvadori, M. Carnevale, and D. Misul, Identification of fluctuation modes for a cylindrical film cooling hole using the spectral proper orthogonal decomposition method, in *Turbo Expo: Power for Land, Sea, and Air*, Vol. 86038 (American Society of Mechanical Engineers, New York, NY, 2022), p. V06AT12A006.
[43] B. Zhang, L. Zhou, K. Tim, L. Wang, J. Niu, and C. Mak, Extended spectral proper orthogonal decomposition for analysis of correlated surrounding flow structures and wind load components of a building, J. Wind Eng. Ind. Aerodyn. **240**, 105512 (2023).

[44] M. Tutkun and W. George, Lumley decomposition of turbulent boundary layer at high Reynolds numbers, Phys. Fluids **29**, 020707 (2017).

[45] L. Perret and F. Kerhervé, Identification of very large scale structures in the boundary layer over large roughness elements, Exp. Fluids **60**, 97 (2019).

[46] S. Anantharamu and K. Mahesh, Analysis of wall-pressure fluctuation sources from direct numerical simulation of turbulent channel flow, J. Fluid Mech. **898**, A17 (2020).

[47] G. Tissot, A. Cavalieri, and É. Mémin, Stochastic linear modes in a turbulent channel flow, J. Fluid Mech. **912**, A51 (2021).

[48] S. Cottier, C. Combs, and L. Vanstone, Spectral proper orthogonal decomposition analysis of shock-wave/boundary-layer interactions, in *Proceedings of the AIAA Aviation Forum* (AIAA, Reston, VA, 2019), p. 3331.

[49] V. Vishwanathan, D. Fritsch, T. Lowe, and W. Devenport, Analysis of coherent structures over a smooth wall turbulent boundary layer in pressure gradient using spectral proper orthogonal decomposition, in *Proceedings of the AIAA Aviation Forum* (AIAA, Reston, VA, 2021), p. 2893.

[50] A. Hamzehloo, D. Lusher, and N. Sandham, Direct numerical simulations and spectral proper orthogonal decomposition analysis of shocklet-containing turbulent channel counter-flows, Int. J. Heat Fluid Flow **104**, 109229 (2023).

[51] F. R. do Amaral and Andre Cavalieri, Coherent pressure structures in turbulent channel flow, Phys. Rev. Fluids **9**, 074606 (2024).

[52] J. Delville, L. Ukeiley, L. Cordier, J.-P. Bonnet, and M. Glauser, Examination of large-scale structures in a turbulent plane mixing layer. Part 1. Proper orthogonal decomposition, J. Fluid Mech. **391**, 91 (1999).

[53] C. Braud, D. Heitz, G. Arroyo, L. Perret, J. Delville, and J.-P. Bonnet, Low-dimensional analysis, using POD, for two mixing layer–wake interactions, Int. J. Heat Fluid Flow **25**, 351 (2004).

[54] J. Weiss, B. Steinfurth, L. Chamard, A. Giani, and P. Combette, Spectral proper orthogonal decomposition of unsteady wall shear stress under a turbulent separation bubble, AIAA J. **60**, 2150 (2022).

[55] E. Thacher, B. Van Ruymbeke, C. Gabillet, N. Jacques, and S. Mäkiharju, Flow topology changes with bubbly flow around a circular cylinder, Int. J. Multiphase Flow **179**, 104917 (2024).

[56] M. Glauser, S. Leib, and W. George, Coherent structures in the axisymmetric turbulent jet mixing layer, in *Turbulent Shear Flows 5* (Springer, Berlin, Heidelberg, 1987), pp. 134–145.

[57] R. Arndt, D. Long, and M. Glauser, The proper orthogonal decomposition of pressure fluctuations surrounding a turbulent jet, J. Fluid Mech. **340**, 1 (1997).

[58] M. Tutkun, P. Johansson, and W. George, Three-component vectorial proper orthogonal decomposition of axisymmetric wake behind a disk, AIAA J. **46**, 1118 (2008).

[59] D. Araya, T. Colonius, and J. Dabiri, Transition to bluff-body dynamics in the wake of vertical-axis wind turbines, J. Fluid Mech. **813**, 346 (2017).

[60] S. Nidhan, K. Chongsiripinyo, O. T. Schmidt, and S. Sarkar, Spectral proper orthogonal decomposition analysis of the turbulent wake of a disk at Re = 50 000, Phys. Rev. Fluids **5**, 124606 (2020).

[61] S. Gordeyev and F. Thomas, Coherent structure in the turbulent planar jet. Part 1. Extraction of proper orthogonal decomposition eigenmodes and their self-similarity, J. Fluid Mech. **414**, 145 (2000).

[62] J. Citriniti and W. George, Reconstruction of the global velocity field in the axisymmetric mixing layer utilizing the proper orthogonal decomposition, J. Fluid Mech. **418**, 137 (2000).

[63] C. Chen, S. Wang, and S. Ghaemi, Spectral proper orthogonal decomposition of time-resolved three-dimensional flow measurements in the turbulent wake of the Ahmed body, J. Fluid Mech. **985**, A19 (2024).

[64] K. Gudmundsson and T. Colonius, Instability wave models for the near-field fluctuations of turbulent jets, J. Fluid Mech. **689**, 97 (2011).

[65] O. Schmidt, A. Towne, T. Colonius, A. Cavalieri, P. Jordan, and G. Bres, Wavepackets and trapped acoustic modes in a turbulent jet: Coherent structure eduction and global stability, J. Fluid Mech. **825**, 1153 (2017).

[66] O. Schmidt, A. Towne, G. Rigas, T. Colonius, and G. Brès, Spectral analysis of jet turbulence, J. Fluid Mech. **855**, 953 (2018).

[67] D. Brouzet, A. Haghiri, M. Talei, M. Brear, O. Schmidt, G. Rigas, and T. Colonius, Role of coherent structures in turbulent premixed flame acoustics, AIAA J. **58**, 2635 (2020).
[68] P. Milani, D. Ching, A. Banko, and J. Eaton, Shear layer of inclined jets in crossflow studied with spectral proper orthogonal decomposition and spectral transfer entropy, Int. J. Heat Mass Transf. **147**, 118972 (2020).
[69] P. A. Kadu, Y. Sakai, Y. Ito, K. Iwano, M. Sugino, T. Katagiri, T. Hayase, and K. Nagata, Application of spectral proper orthogonal decomposition to velocity and passive scalar fields in a swirling coaxial jet, Phys. Fluids **32**, 015106 (2020).
[70] K. Geigle, M. Köhler, W. O'Loughlin, and W. Meier, Investigation of soot formation in pressurized swirl flames by laser measurements of temperature, flame structures and soot concentrations, Proc. Combust. Inst. **35**, 3373 (2015).
[71] J. Cheng, Y. Tang, W. Han, and L. Yang, A review of soot formation and evolution in turbulent swirling flames, J. Aerosol Sci. **190**, 106667 (2025).
[72] S. Pope, *Turbulent Flows* (Cambridge University Press, Cambridge, UK, 2000).
[73] M. Germano, U. Piomelli, P. Moin, and W. Cabot, A dynamic subgrid-scale eddy viscosity model, Phys. Fluids **3**, 1760 (1991).
[74] C. Eberle, P. Gerlinger, K. Geigle, and M. Aigner, Soot predictions in an Aero-Engine model combustor at elevated pressure using URANS and finite-rate chemistry, in *Proceedings of the 50th AIAA/ASME/SAE/ASEE Joint Propulsion Conference* (AIAA, Inc., Cleveland, OH, 2014), p. 3472.
[75] M. Grader and P. Gerlinger, Influence of operating conditions on flow field dynamics and soot formation in an aero-engine model combustor, Combust. Flame **258**, 112712 (2023).
[76] S. Chong, V. Raman, M. Mueller, P. Selvaraj, and H. Im, Effect of soot model, moment method, and chemical kinetics on soot formation in a model aircraft combustor, Proc. Combust. Inst. **37**, 1065 (2019).
[77] B. Franzelli, A. Vié, and N. Darabiha, A three-equation model for the prediction of soot emissions in LES of gas turbines, Proc. Combust. Inst. **37**, 5411 (2019).
[78] J. Garcia-Oliver, J. Pastor, I. Olmeda, A. Kalbhor, D. Mira, and J. van Oijen, LES of a pressurized sooting aero-engine model burner using a computationally efficient discrete sectional method coupled to tabulated chemistry, Combust. Flame **260**, 113198 (2024).
[79] M. Mueller and H. Pitsch, Large eddy simulation of soot evolution in an aircraft combustor, Phys. Fluids **25**, 110812 (2013).
[80] C. Pierce and P. Moin, Progress-variable approach for large-eddy simulation of non-premixed turbulent combustion, J. Fluid Mech. **504**, 73 (2004).
[81] M. Ihme and H. Pitsch, Modeling of radiation and nitric oxide formation in turbulent nonpremixed flames using a flamelet/progress variable formulation, Phys. Fluids **20**, 055110 (2008).
[82] G. Arumapperuma, Y. Tang, A. Attili, and W. Han, Spectral analysis of soot dynamics in an aero-engine model combustor, Proc. Combust. Inst. **40**, 105344 (2024).
[83] R. Barlow, A. Karpetis, J. Frank, and J. Chen, Scalar profiles and NO formation in laminar opposed-flow partially premixed methane/air flames, Combust. Flame **127**, 2102 (2001).
[84] R. Bilger, The structure of turbulent nonpremixed flames, in *Proceedings of the International Symposium on Combustion* (Elsevier, Amsterdam, 1989), Vol. 22, pp. 475–488.
[85] K. Narayanaswamy, G. Blanquart, and H. Pitsch, A consistent chemical mechanism for oxidation of substituted aromatic species, Combust. Flame **157**, 1879 (2010).
[86] G. Blanquart, P. Pepiot-Desjardins, and H. Pitsch, Chemical mechanism for high temperature combustion of engine relevant fuels with emphasis on soot precursors, Combust. Flame **156**, 588 (2009).
[87] A. Felden, E. Riber, and B. Cuenot, Impact of direct integration of analytically reduced chemistry in LES of a sooting swirled non-premixed combustor, Combust. Flame **191**, 270 (2018).
[88] L. Gallen, A. Felden, E. Riber, and B. Cuenot, Lagrangian tracking of soot particles in LES of gas turbines, Proc. Combust. Inst. **37**, 5429 (2019).
[89] M. Frenklach, Method of moments with interpolative closure, Chem. Eng. Sci. **57**, 2229 (2002).
[90] P. Koob, H. Nicolai, R. Schmitz, and C. Hasse, Analysis of potential soot breakthrough during oxidation at aero-engine relevant conditions, Proc. Combust. Inst. **40**, 105672 (2024).

[91] F. Gelbard and J. Seinfeld, Simulation of multicomponent aerosol dynamics, J. Colloid Interface Sci. **78**, 485 (1980).

[92] M. Mueller, G. Blanquart, and H. Pitsch, Hybrid method of moments for modeling soot formation and growth, Combust. Flame **156**, 1143 (2009).

[93] M. Mueller, G. Blanquart, and H. Pitsch, A joint volume-surface model of soot aggregation with the method of moments, Proc. Combust. Inst. **32**, 785 (2009).

[94] H. Wang and M. Frenklach, A detailed kinetic modeling study of aromatics formation in laminar premixed acetylene and ethylene flames, Combust. Flame **110**, 173 (1997).

[95] M. E. Mueller and H. Pitsch, Large eddy simulation subfilter modeling of soot-turbulence interactions, Phys. Fluids **23**, 115104 (2011).

[96] I. Gatin, V. Vukčević, H. Jasak, and H. Rusche, Enhanced coupling of solid body motion and fluid flow in finite volume framework, Ocean Eng. **143**, 295 (2017).

[97] P. Welch, The use of fast Fourier transform for the estimation of power spectra: A method based on time averaging over short, modified periodograms, IEEE Trans. Audio Electroacoust. **15**, 70 (1967).

[98] G. Mengaldo and R. Maulik, PySPOD: A Python package for spectral proper orthogonal decomposition (SPOD), J. Open Source Software **6**, 2862 (2021).